molecules

MDPI

Article

Optimization of Sintering Conditions to Enhance the Dielectric Performance of Gd^{3+} and Ho^{3+} Codoped $BaTiO_3$ Ceramics

Jianghui Bai [1], Qiaoli Liu [2], Xia Li [3], Xin Wei [2] and Liping Li [1,*]

[1] State Key Lab of Inorganic Syntheses and Preparative Chemistry, College of Chemistry, Jilin University, Changchun 130012, China
[2] Key Laboratory for Special Functional Materials at Jilin Provincial Universities, Jilin Institute of Chemical Technology, Jilin 132022, China
[3] Innovation Center for Chemical Science, College of Chemistry, Chemical Engineering and Materials Science, Soochow University, Suzhou 215123, China
* Correspondence: author: lipingli@jlu.edu.cn

Abstract: $BaTiO_3$ dielectric capacitors, one of the important energy storage devices, play critical roles in storing electricity from renewable energies of water, wind, solar, etc. The synthesis of $BaTiO_3$ ceramics with weak temperature dependence and a high dielectric constant at room temperature (ε_{RT}') is an urgent problem to meet the miniaturization and large capacity of dielectric capacitors. Doping rare earth elements into $BaTiO_3$ can solve this problem, but it is still challenging. In this work, we adopt a synergistic strategy of increasing ε_{RT}' and improving the temperature stability by codoping Gd^{3+} and Ho^{3+}, respectively, to address this challenge. By carefully adjusting the synthesis conditions in the solid-state reaction, codoping 7% Gd^{3+} and 7% Ho^{3+} in $BaTiO_3$ (BGTH7) ceramics were synthesized. The temperature-dependent dielectric constant reveals that the obtained optimal BGTH7 ceramic satisfies the X7U specification and displays a stable ε' in the temperature range of −55~125 °C. The optimal BGTH7 ceramic after sintering at 1400 °C for 6 h exhibits a high dielectric constant of 5475 and low dielectric loss (tan δ) of 0.0176, hitherto exhibiting the best performance in X7U ceramics. The findings in this work are conducive to the miniaturization and stabilization of dielectric energy storage devices.

Keywords: energy storage; sintering conditions; dielectric ceramics; Gd^{3+}; Ho^{3+}; $BaTiO_3$

Citation: Bai, J.; Liu, Q.; Li, X.; Wei, X.; Li, L. Optimization of Sintering Conditions to Enhance the Dielectric Performance of Gd^{3+} and Ho^{3+} Codoped $BaTiO_3$ Ceramics. *Molecules* **2022**, *27*, 7464. https://doi.org/10.3390/molecules27217464

Academic Editors: Zhengpei Miao, Zhenye Kang and Xinlong Tian

Received: 23 September 2022
Accepted: 31 October 2022
Published: 2 November 2022

1. Introduction

The limited amount of fossil fuels raise much attention about the development of renewable resources [1,2]. The conversion of renewable energy sources into electrical energy and efficient power storage are essential to solve the energy crisis [3,4]. Commonly used electrical energy storage devices are lithium batteries, supercapacitors, and dielectric capacitors. The low release power of lithium batteries and the instability of supercapacitors restrict their application in energy storage [5]. Among the dielectric energy storage materials, lead-free $BaTiO_3$ dielectric capacitors are attracting attention for overcoming the above-mentioned disadvantages, exhibiting ultra-fast charge/discharge capability and high temperature tolerance [6,7].

The capacitance (C) of dielectric capacitors is governed by the dielectric constant (ε'), capacitance plate area (S), and distance between two pole plates (d), as shown in the formulas below:

$$C = \varepsilon' S / 4\pi \mathrm{k} d \qquad (1)$$

k is the electrostatic force constant (k = 8.987551×10^9 N·m^2/C^2). $BaTiO_3$ dielectric ceramics are a key component of dielectric energy storage capacitors. However, the unstable and low capacity of $BaTiO_3$ dielectric capacitors cannot meet the demand for miniaturization and the high performance of dielectric capacitors [8]. Therefore, obtaining a stable and high dielectric constant near the room temperature (ε'_{RT}) for $BaTiO_3$ ceramics can meet the requirements of miniaturization and high performance of dielectric capacitors, which are more widely used in miniaturized and integrated circuit systems [9,10].

In previous studies, significant efforts have been made to address the issues mentioned above. Tetragonal $BaTiO_3$ has large spontaneous polarization and high ε', eventually increasing the energy density [11,12]. Ma et al. prepared $BaTiO_3$-La_2O_3-SiO_2 particles. More La^{3+} and Si^{4+} ions incorporated into the $BaTiO_3$ lattice with increasing SiO_2 enhanced spontaneous polarization and resulted in increased energy density [13].

During the tetragonal to the cubic transition of $BaTiO_3$ at 120 °C, ε' increases sharply, forming a dielectric peak [14]. Shifting the dielectric peak temperature (T_m) to room temperature contributes to high ε'_{RT}. Gd-doped $BaTiO_3$ can significantly reduce the T_m and increase ε_{RT}' [15,16]. Gd-doped $0.7BaTiO_3$-$0.3Sr_{0.2}Bi_{0.7}TiO_3$ ceramics possess high ε'_{RT} ($\varepsilon'_{RT} \approx 4000$) and T_m near -19 °C, exhibiting excellent energy storage. The difference in the valence of ions at the A-site induces a decreased tolerance factor, resulting in a decrease in T_m [17].

Moreover, the incorporation of Ho in $BaTiO_3$ can broaden the dielectric peak and obtain stable dielectric constant [18]. In recent research reports, Hu [19] successfully synthesized Bi_2O_3 and Ho_2O_3 codoped $BaTiO_3$-based ceramics by a solid-phase method, with a stable ε' between 2400 and 2600 and satisfactory temperature stability of capacitance with an X8R dielectric specification. La-, Pr-, Nd-, Sm-, and Ho- codoped $BaTiO_3$ all had wide dielectric peaks, satisfying the dielectric specifications of X5T, X6T, X7T, and X8S, respectively [20].

Although the dielectric performance was enhanced using the method reported above for $BaTiO_3$, doping Gd or Ho alone is not sufficient to increase ε'_{RT} and stable ε' in the temperature range of operation. The dielectric performance of doped ceramics is also dependent on sintering temperature (T_s) and dwell time (t_d). Therefore, we propose a synergistic strategy codoping 7% Gd^{3+} and 7% Ho^{3+} in $BaTiO_3$ (BGTH7), carefully adjusting the synthesis conditions by the solid-phase method to obtain high ε'_{RT} and stable ε', achieving stable and high capacities for $BaTiO_3$ dielectric capacitors. The specific roadmap was shown in Figure 1.

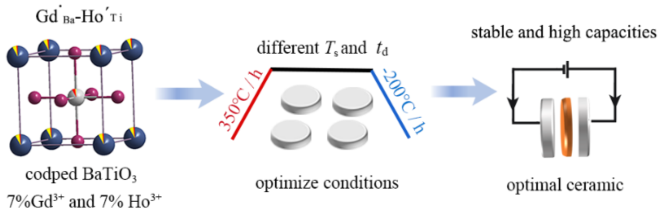

Figure 1. Target roadmap for high and stable capacitance achievement.

In this work, the phase structure of BGTH7 ceramics was studied by X-ray diffraction and Raman spectroscopy. The improved performance with dielectric diffuse phase transition behavior can be obtained from dielectric measurement. The shift of T_m was caused by the charge-coupled substitution of Gd^{3+} and Ho^{3+} at both Ba and Ti sites, which was confirmed by X-ray photoelectron spectroscopy (XPS), electron paramagnetic resonance (EPR), and Raman spectrum. The scanning electric microscope (SEM) images show that optimizing T_s can improve the density and average grain size of the ceramic samples. Eventually, high ε'_{RT} and stable ε' at work temperature can be obtained, which is promising for miniaturization and high performance of devices.

2. Results and Discussion

2.1. Effect of Sintering Temperature and Dwell Time on Phase Purity and Morphology

Gd^{3+} and Ho^{3+} codoped $BaTiO_3$ ceramics were synthesized by a solid-state method to achieve a high ε'_{RT} and stable ε' in the operating temperature range. Usually, the sintering temperature (T_s) and dwell time (t_d) greatly affect the phase composition in solid-phase reactions. Thus, we systematically adjusted T_s and t_d to optimize the sintering conditions

(Figure 2a). Two BGTH7 ceramics after sintering at T_s = 1200 and 1300 °C contained impurity phases $Ba_{12}Ho_{4.67}Ti_8O_{35}$ (PDF # 43−0420) and Ho_2O_3 (PDF # 43−1018) (marked with * and # in Figure 2b, respectively). Sintering at low temperatures makes it difficult to incorporate Ho^{3+} into the perovskite structure owing to the large radius of Ho^{3+} (0.901 Å) in octahedral coordination compared to that of Ti^{4+} (0.605 Å) [21]. And as shown in Figure S1, ceramics sintered at 1200 and 1300 °C exhibited low density and small grain size. High T_s can change the boundary of the phase diagram in multiple composition compounds but also increase the solution limit of doped ions in perovskite [22]. Thus, at T_s = 1400 °C, BGTH7 ceramics exhibited a pure phase of perovskite.

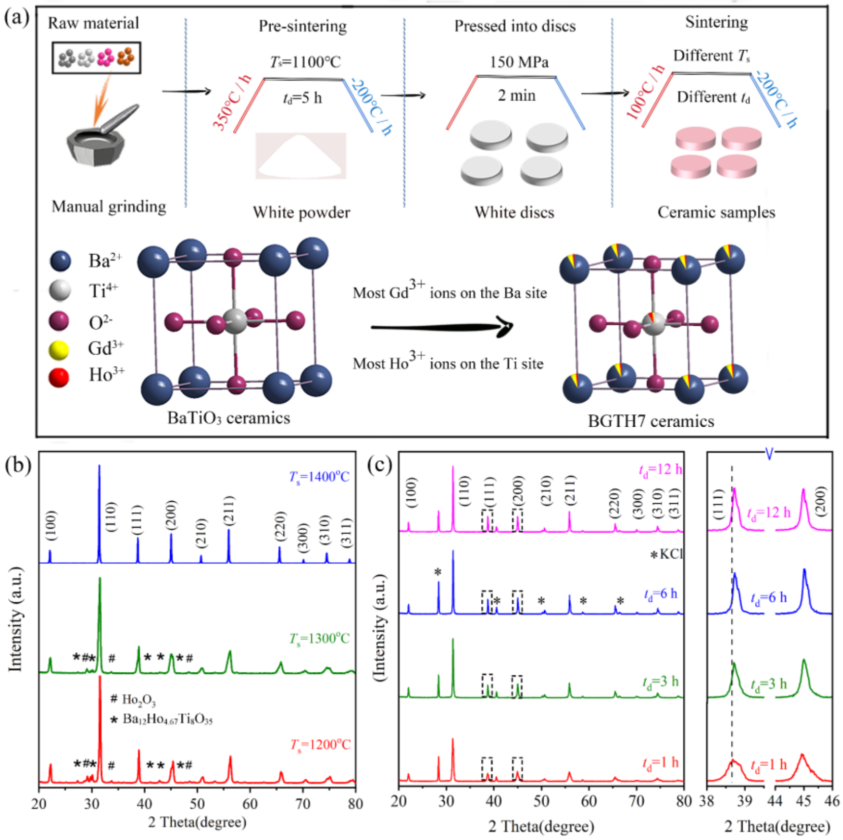

Figure 2. (**a**) Schematic illustration of the synthesis of BGTH7 ceramic samples. (**b**) X-ray diffraction patterns of the BGTH7 ceramics sintered at different sintering temperatures (T_s) for 12 h. (**c**) X-ray diffraction patterns of BGTH7 ceramics sintered for different dwell times (t_d) at 1400 °C. The right panel shows the enlarged diffraction peaks of (111) and (200) in the 2θ ranges of 38–39.5° and 44–46°, respectively.

The phase structure of BGTH7 ceramics sintered at 1400 °C with different t_d was examined by XRD. BGTH7 ceramics sintered for different t_d (1, 3, 6, 12 h) are pure phases, as shown in Figure 2c. As t_d increased, the XRD peaks gradually narrowed, and their intensities were enhanced, demonstrating an improvement in crystallinity. To accurately determine the shift of the peak, the internal standard KCl was added to the BGTH7 ceramic powder. The enlarged peak at approximately 38° slightly shifted toward a higher 2θ angle as t_d increased, confirming a slight contraction in unit cell volume (V_0). Notably, the diffraction peak (200) at approximately 45° for all ceramics did not show any splitting, which may be attributed to the cubic structure, similar to cubic $BaTiO_3$ (PDF # 31−0174). Certainly, a slight distortion in the tetragonal phase structure or broadening of the XRD peaks can also obscure such a splitting, and this obscuring effect is difficult to detect by XRD. Therefore, in addition to XRD data, spectroscopic evidence could be helpful to prove the accurate phase structure of BGTH7 ceramics sintered at 1400 °C.

Raman spectroscopy can effectively distinguish the tetragonal or cubic phase of perovskite. Ideal cubic perovskite with $Pm\bar{3}m$ does not give any Raman signal due to a centrosymmetric structure belonging to the O_{1h} space group [23]. Once the $BaTiO_3$ structure deviates from cubic symmetry, such as tetragonal with $P4mm$, four degenerate $3F_{1u}$ (IR) + F_{2u} (inactive) modes for the O_{1h} space group split into eight Raman active $3A_1 + B_1 + 4E$ modes [24]. Thus, the Raman signal can be observed.

As shown in Figure 3a, one peak at approximately 310 cm^{-1}, usually from the B_1 and E modes, was seen in the Raman spectra of sintered BGTH7 ceramics (t_d = 1 3, 6, 12 h), indicating that BGTH7 ceramics sintered at 1400 °C had a tetragonal structure [25,26]. Different from the sharp peak for the ceramics that underwent long dwell times, the peak at 310 cm^{-1} was not obvious for the BGTH7 ceramic sintered at t_d = 1 h due to incomplete grain growth. With these observations in mind, we refined the XRD data of BGTH7 ceramics sintered at 1400 °C by the tetragonal phase structure. The obtained lattice parameters in Table S1 show that the values of a and c are very close ($a = b \neq c$, $\alpha = \beta = \gamma = 90°$), i.e., the structure of BGTH7 ceramics sintered at 1400 °C slightly deviates from cubic symmetry. On the other hand, the Raman peak at approximately 520 cm^{-1} in Figure 3a corresponds to distorted $(TiO_6)^{4-}$ octahedra, confirming the presence of a small structure distortion. A similar distortion was also observed in previous reports [27,28]. The tetragonal phase structure of BGTH7 ceramics sintered at 1400 °C can have large spontaneous polarization and a high ε', which is desirable for $BaTiO_3$ dielectric energy storage capacitors [29,30].

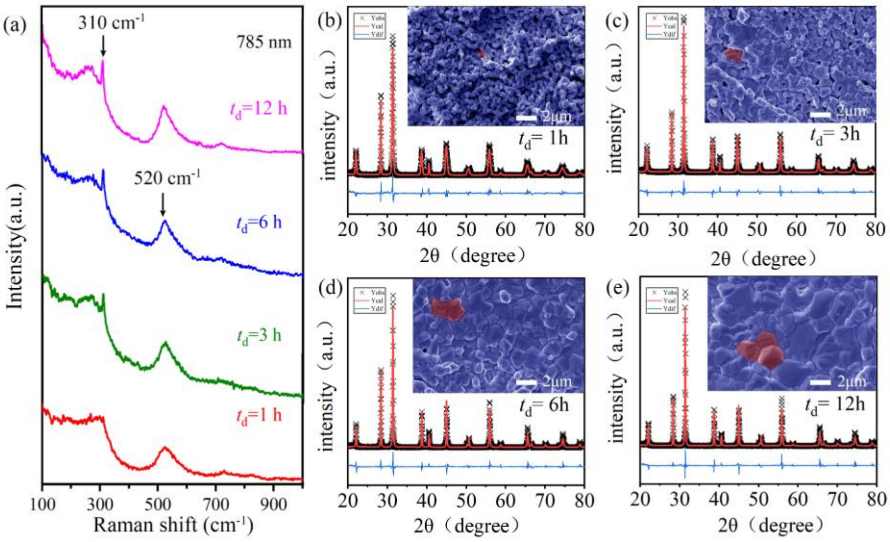

Figure 3. (**a**) Room-temperature Raman spectra in the low-wavenumber region of 100−1000 cm^{-1} for BGTH7 powder sintered for different t_d at T_s = 1400 °C. The results of the XRD refinement and SEM images for BGTH7 ceramics sintered with different t_d at T_s = 1400 °C. (**b**) t_d = 1 h, (**c**) t_d = 3 h, (**d**) t_d = 6 h, (**e**) t_d = 12 h.

The dwell time greatly affected the morphology of intact disc BGTH7 ceramics sintered at 1400 °C. According to the grain size analysis in Figure S2, the average grain sizes of the BGTH7 ceramics were approximately 0.71, 1.15, 2.11, and 3.17 µm for t_d = 1, 3, 6, and 12 h, respectively. As illustrated by the SEM images in the inset of Figure 3b–e, the BGTH7 ceramic after dwelling for t_d = 1 h exhibited tiny grains and pores, showing incomplete grain growth. The grain size was improved by prolonging the dwell time. These gradually increased grains filled the pores, resulting in a denser microstructure. The relative density (ρ_r) of the BGTH7 ceramics was 73, 79, 86, and 93%, sintered at 1400 °C for t_d = 1, 3, 6, and 12 h, respectively, in which ρ_r was estimated using the following formula:

$$\rho_r = \rho_a / \rho_0 \tag{2}$$

ρ_0 is the theoretical density obtained from Rietveld refinement, and ρ_a is the actual bulk density that can be measured using the Archimedes method.

2.2. Effect of Dwell Time on the Site Occupation of BGTH7 Ceramics Sintered at 1400 °C

Rare earth ions, such as Gd^{3+} and Ho^{3+}, have different ion radii than Ba^{2+} and Ti^{4+}, which often leads to their preferential occupation once they are doped in $BaTiO_3$. Such a preferential occupation has an important influence on the dielectric property. In addition to the ionic radius, some other factors can also change the occupation of rare earth ions in the perovskite, such as the valence state of Ti and oxygen vacancies, which can be determined by XPS, EPR, and photoluminescence analysis.

The valence state of Ti ions was investigated by XPS. Figure 4a and Figure S3 shows the Ti 2p core level spectra of BGTH7 sintered at T_s = 1400 °C. Well spin-orbital splitting peaks Ti2$p_{3/2}$ (at approximately 457.8 eV) and Ti2$p_{1/2}$ (at approximately 463.6 eV) were observed, and the splitting energy of 2$p_{3/2}$ and 2$p_{1/2}$ was 5.8 eV, confirming the presence of Ti^{4+} ions [31,32]. Generally, the characteristic peak of Ti^{3+} 2$p_{3/2}$ appears at approximately 455 eV [33]. Deconvolution analysis showed that there was the absence of a peak at 455 eV, proving the absence of Ti^{3+}, i.e., only one oxidation state Ti^{4+} in the BGTH7 ceramics sintered at 1400 °C.

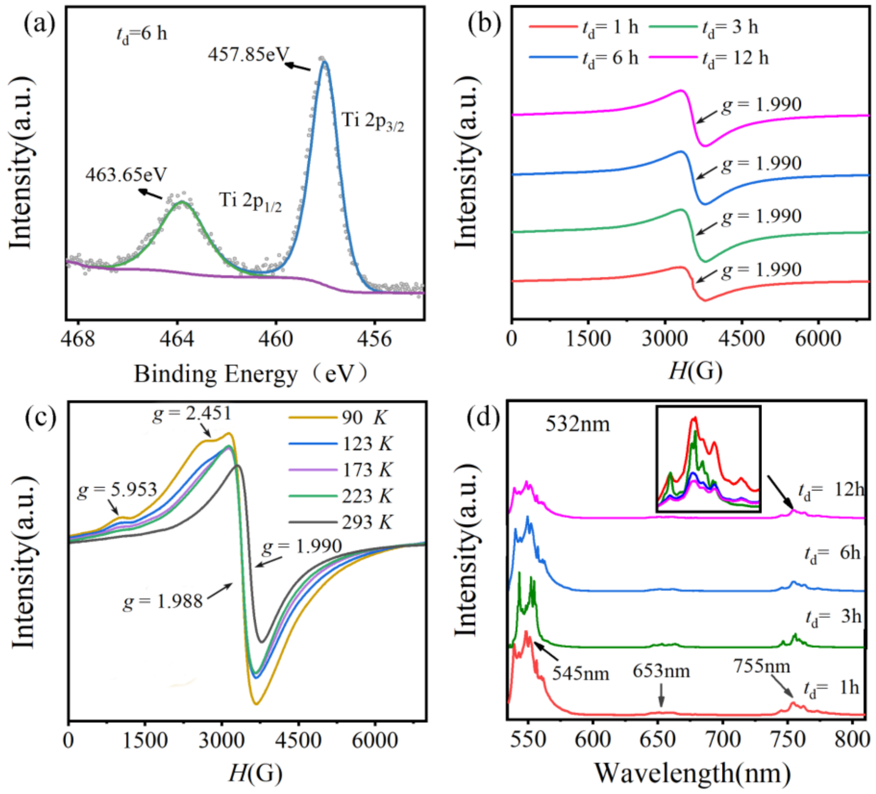

Figure 4. (**a**) Ti 2p XPS spectrum of BGTH7 sintered at T_s = 1400 °C for 6 h. (**b**) EPR spectra of BGTH7 sintered at T_s = 1400 °C measured at room temperature. (**c**) Temperature-dependent EPR spectra of BGTH7 sintered at T_s = 1400 °C for 6 h. (**d**) Raman spectra under 532 nm excitation of BGTH7 ceramics sintered at T_s = 1400 °C for 1, 3, 6 and 12 h.

Due to the charge difference between dopant ions Gd^{3+}/Ho^{3+} and host ions Ba^{2+} and Ti^{4+} in $BaTiO_3$, the incorporation of Gd^{3+}/Ho^{3+} could introduce a positive or negative charge center. These charge mismatches can be compensated by vacancies, described as follows by the Kröger–Vink notation:

$$Ln_2O_3 \xrightarrow{BaTiO_3} 2Ln_{Ba}^{\bullet} + V_{Ba}'' + 3O_O^x \quad (3)$$

$$Ln_2O_3 \xrightarrow{BaTiO_3} 2Ln_{Ti}' + V_O^{\bullet\bullet} + 3/2\,O_2(g) \quad (4)$$

Here, Ln represents Gd^{3+} or Ho^{3+}. V_{Ba}'' and $V_O^{\bullet\bullet}$ usually displays EPR signals at g = 1.974 and 1.955 [34,35]. In Figure 4b, only a broad and symmetrical signal with g = 1.990 was observed for BGTH7 ceramics sintered at 1400 °C. This signal is attributed to Gd^{3+} with an electron configuration of $4f^7$ (ground state is $^8S_{7/2}$) [36]. The EPR spectrum of Gd^{3+} is highly dependent on the symmetry of ion coordination in Figure S4. New weak signals appeared with g = 5.953 and 2.451 at temperatures below 223 K in Figure 4c, which is associated with the change in Gd^{3+} symmetry from slightly distorted cubic coordination to intermediate coordination because of the increased structure distortion at a low temperature [37,38]. The absence of a signal related to V_{Ba}'' or $V_O^{\bullet\bullet}$ indicates the absence of vacancies. As is well known, performing EPR operations under ultrahigh vacuum and at low temperatures can increase the detection limit. Variable temperature EPR spectroscopy was investigated for the BGTH7 ceramic sintered at 1400 °C for 6 h. As illustrated in Figure 4c, the vacancy signals were not activated when the temperature was changed through T_m (270.36 K). Therefore, the incorporation of Gd^{3+} and Ho^{3+} could adopt a charge-coupled substitution on both the Ba and Ti sites:

$$Ln_2O_3 \overset{BaTiO_3}{\rightarrow} Ln_{Ba}^{\bullet} + Ln_{Ti}^{'} + 3O_O^x \quad (5)$$

Ho^{3+} ions in some perovskites exhibit a strong photoluminescence emission. The Raman spectrum of Ho^{3+} doped $BaTiO_3$ under 532 nm excitation is often used to probe the site occupations of Ho^{3+} ions because the concentration of Ho^{3+} ions on the Ba sites is highly dependent on the transition intensities of $^5F_4/^5S_2 \rightarrow {}^5I_8$ at 545 nm, $^5F_5 \rightarrow {}^5I_8$ at 653 nm, and $^5F_4/^5S_2 \rightarrow {}^5I_7$ at 755 nm [21,39]. Figure 4d and Figure S5 display the Raman spectra of BGTH7 ceramics sintered at 1400 °C under 532 nm excitation. Taking the transition intensity at 755 nm as a comparison for the inset in Figure 4d, the concentration of Ho^{3+} at the Ba site can be estimated [17]. For BGTH7 ceramics with t_d values of 1, 3, 6, and 12 h, the contents of Ho^{3+} substituted for Ba^{2+} were 0.0059, 0.0050, 0.0022, and 0.0018, respectively. Increasing the dwell time at a high temperature (1400 °C) could reduce the incorporation of Ho^{3+} into the Ba site. The cross-site occupancy between Gd^{3+} and Ho^{3+} is described in Equation (5) and occurred in BGTH7 ceramics sintered at 1400 °C. Therefore, for BGTH7 ceramics with t_d values of 1, 3, 6, and 12 h, the contents of Ho^{3+} substituted for Ti^{4+} were 0.0641, 0.065, 0.0678, and 0.0682, respectively. From the ionic radius in Table S2, Gd^{3+} ions preferentially incorporated into the Ba site, while Ho^{3+} preferentially incorporated into the Ti site, forming a $Gd_{Ba}^{\bullet}$-$Ho_{Ti}^{'}$ complex. On the other hand, a small quantity of Ho^{3+} and Gd^{3+} change their occupation on the Ba site and Ti site to $Ho_{Ba}^{\bullet}$-$Gd_{Ti}^{'}$ according to photoluminescence analysis. When the sintering conditions were T_s = 1400 °C and t_d = 6 h, the real molecular formula of the obtained ceramic was $(Ba_{0.93}Gd_{0.0678}Ho_{0.0022})(Ti_{0.93}Ho_{0.0678}Gd_{0.0022})\,O_3$, having more $Gd_{Ba}^{\bullet}$-$Ho_{Ti}^{'}$ complexes.

2.3. Dielectric Properties of BGTH7 Ceramics Sintered at 1400 °C

The Electronic Industry Association (EIA) classifies class II ceramic capacitors into two categories: capacitance-stable and high-capacitance ceramic capacitors. The most commonly used capacitance-stable capacitors are R-type capacitors. Over the operating temperatures, the capacitance change of R-type capacitors does not exceed 15%. However, these capacitors have relatively low dielectric constant, which are not suitable for miniaturized applications in electronic products. Another capacitor is the Y-type capacitor. Even though the Y-type capacitor has a high capacitance compared to the R-type capacitor, it is difficult to apply because of its unstable dielectric constant. A U-type capacitor combines the advantages of temperature stability and high capacitance, eventually having a stable and high dielectric constant over the entire operating temperature range [40–43].

Table S3 lists EIA classification of Class II capacitors. Figure 5a–d shows the temperature dependence of the ε' and dielectric loss (tan δ) measured at 1 kHz for BGTH7 ceramics sintered at 1400 °C. According to Table S3, BGTH7 ceramics (t_d = 1, 3, 6, 12 h) satisfy the X8R, X7U, X7U, and X6U specifications, respectively. The dielectric properties for all BGTH7 ceramics are shown in Table S4. In particular, the BGTH7 ceramic sintered for 6 h at 1400 °C exhibits high ε'_{RT} ($\varepsilon'_{RT} > 5000$) and ultralow tan δ (tan $\delta < 0.02$), with the location of the dielectric peak near the room temperature. This finding is very important for solving the problem of the location of the dielectric peak for conventional $BaTiO_3$ ceramics being too high (close to 125 °C) to satisfy the requirement of the development and application of small electronics at room temperature.

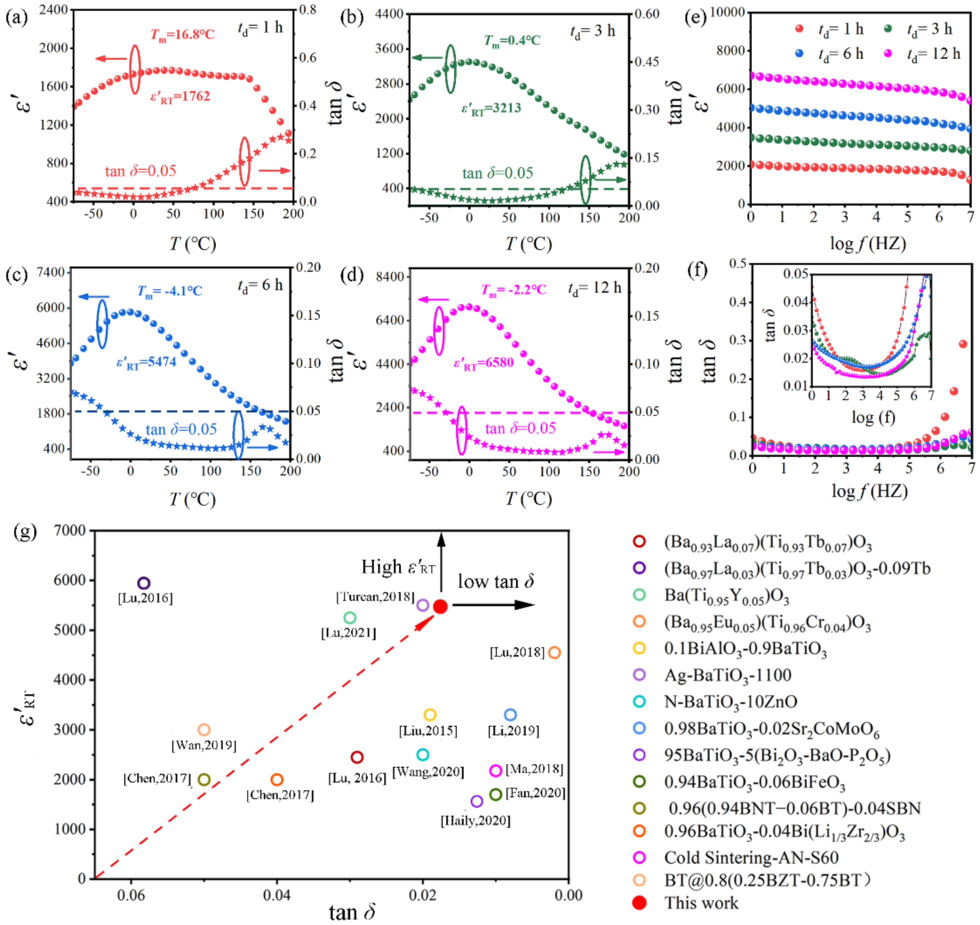

Figure 5. Temperature dependence of the dielectric constant (ε') and dielectric loss (tan δ) measured at 1 kHz for BGTH7 ceramics sintered at T_s = 1400 °C for different t_d. (**a**) t_d = 1 h, (**b**) t_d = 3 h, (**c**) t_d = 6 h, (**d**) t_d = 12 h. The frequency dependence of the dielectric constant (ε') and dielectric loss (tan δ) was measured at room temperature for BGTH7 ceramics sintered at T_s = 1400 °C for different t_d (**e**) and (**f**). (**g**) The dielectric properties of this work are compared with those of previously reported $BaTiO_3$-based dielectric ceramics with X7U specifications [2,44–55].

ε' and tan δ of BGTH7 ceramics sintered at 1400 °C with different t_d exhibited the same changes with frequency (Figure 5e,f). The value of ε' in the high frequency region is lower than the low frequency region. The variation in ε' with frequency can be interpreted by the Maxwell–Wagner's two-layer models. The total polarization contributes to a high ε' value at low frequency, while in the high-frequency region, dipole inversion fails to keep up with the changing electric field, causing ε' to decrease.

Ceramics sintered at 1200 and 1300 °C exhibited low dielectric constant and high tan δ, as shown in Figures S6 and S7. Dielectric measurements demonstrated that the optimal

BGTH7 ceramic sintered at T_s = 1400 °C and t_d = 6 h possesses high ε'_{RT} (ε'_{RT} = 5475) and low tan δ (tan δ = 0.0176) at 1 kHz, as well as enhanced frequency stability from 1 to 10^7 Hz. In addition, this BGTH7 ceramic satisfied the X7U specification according to Table S4, having stable ε' in the operating temperature range (−55~125 °C). As shown Table S5 and Figure 5g, the BGTH7 ceramic is superior to the X7U specification reported previously, having potential application in microminiature and temperature-stable $BaTiO_3$ dielectric energy storage capacitors.

2.4. Understanding the Excellent Dielectric Properties of BGTH7 Ceramics Sintered at 1400 °C

2.4.1. High Dielectric Constant at Room Temperature

ε'_{RT} gradually increases from 1762 to 6580 as the average grain size changes from 0.71 to 3.17 µm (ρ_r from 73% to 93%, respectively), as shown in Figure S8. The reason for increasing ε'_{RT} can be understood from the following two points: (1) Air acts as a stress snubber and reduces the entrapment forces between grains in the $BaTiO_3$ ceramic, resulting in the formation of pores. Polarization is a critical factor in improving the dielectric constant. Normally, polarization is weakened by the depolarization field that occurs near the pores, resulting in decreasing dielectric constant [56]. High ρ_r shields the depolarization field, resulting in a high ε' of ceramics. Among the four examined BGTH7 ceramics sintered at 1400 °C, the one sintered at t_d = 12 h, having ρ_r as high as 93%, gives the highest ε'_{RT} of 6580. (2) An easier and more regular motion of the domain wall can also increase ε'_{RT} [57,58]. Generally, large grains are conducive to forming orderly dipole alignment and promoting regular domain wall motion, thus increasing ε'. As the grain sizes increased, the dielectric peak was gradually enhanced, resulting in an increased dielectric constant (ε'_{RT}) at room temperature. Therefore, a denser structure and large grain size are beneficial to obtaining high ε'_{RT} in BGTH7 ceramics sintered at 1400 °C.

2.4.2. Shift of the Dielectric Peak

The Goldschmidt tolerance factor (t) can predict the symmetry of ABO_3 perovskites that significantly affect their dielectric performance and is defined as the ratios of the constituent ionic radii of A, B, and O:

$$t = r_A + r_O \ / \ \sqrt{2}\left(r_B + r_O\right) \tag{6}$$

For pure $BaTiO_3$, ${r_{Ba}}^{2+}$, ${r_{Ti}}^{4+}$, and ${r_O}^{2-}$ are 1.61 (in 12 coordinate), 0.605 (in octahedral coordination), and 1.4 Å; thus, $t \approx 1.06$. A previous investigation has shown that the dielectric peak temperature (T_m) of $BaTiO_3$ is highly dependent on the tolerance factor (t). Reducing t can shift the T_m to a lower temperature [59]. When some Gd^{3+} ions are incorporated into Ba sites, the decrease in t shifts T_m to a low temperature. Instead, the substitution of Ho^{3+} for Ti^{4+} ions leads to T_m moving toward higher temperatures, similar to the incorporation of Ca^{2+} [21]. In other words, the charge-coupled substitution of Gd^{3+} and Ho^{3+} at both Ba and Ti sites (Equation (5)) has different effects on T_m, which was caused by the different effects of substitution for Gd^{3+} and Ho^{3+} on Ti-O octahedral distortion [60]. The photoluminescence analysis in Figure 4d indicated that the Ho^{3+} content in the Ti site increases. Consequently, T_m first decreased and then increased, as shown in Figure S9.

All studied BGTH7 ceramics sintered at 1400 °C exhibit dielectric diffusion phase transition (DPT) behavior. The broadening dielectric peak was related to the grain size, which is consistent with numerous past reports [61,62]. In addition, Gd^{3+} and Ho^{3+} codoped $BaTiO_3$ ceramics can also broaden the dielectric peak, similar to La-, Pr-, Nd-, Sm-, and Ho-codoped $BaTiO_3$ ceramics [20]. Codoping of Ho^{3+} with Gd^{3+} has an important effect on the stability of ε' over a wide temperature range.

The detailed mechanisms for improving dielectric properties is illustrated in Figure 6. Charge-coupled substitution of Gd^{3+} and Ho^{3+} at both Ba and Ti sites, decrease of tolerance factor, distortion of octahedral, as well as increased density can be optimized by adjusting sintering temperature, and time. Eventually, the optimal BGTH7 ceramic not only exhibited high ε'_{RT} but also dielectric DPT, which can ensure stable operation for $BaTiO_3$ dielectric energy storage capacitors.

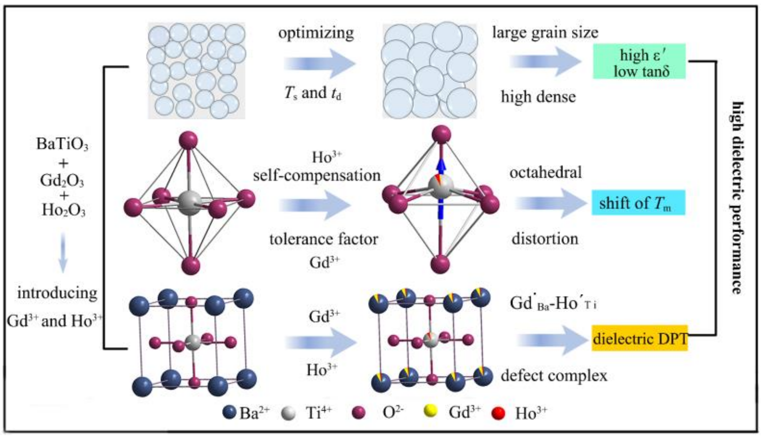

Figure 6. The mechanisms for improving dielectric properties.

3. Materials and Methods

$BaCO_3$ (99.5%), TiO_2 (99.5%), Ho_2O_3 (99.95%), and Gd_2O_3 (99.90%) were used as raw materials, weighed according to 7% Gd^{3+} and 7% Ho^{3+} codoping in $BaTiO_3$ (BGTH7), and milled. After drying and calcining at 1100 °C for 5 h for decarburization, the obtained powder was reground and pressed into discs with a diameter of 12 mm and a thickness of 2 mm at 150 MPa using an aqueous solution of PVA (12% by mass) as a binder. The final sintering conditions to form the BGTH7 ceramics were chosen as heating up directly from room temperature to different T_s (1200 °C $\leq T_s \leq$ 1400 °C, t_d = 12 h) and different t_d (1 h $\leq t_d \leq$ 12 h, T_s = 1400 °C) in the air at a heating rate of 100 °C/h, a cooling rate of −200 °C/h to 700 °C, and then furnace cooling to room temperature.

The crystallographic structures were studied by using X-ray diffraction (XRD: DX-2700, Dandong Haoyuan, Dandong, China) with Cu Kα_1 radiation (λ = 1.540562 Å). The microstructure of the sintered samples was observed using an EVOMA 10 scanning electric microscope (SEM: EVO MA10, Zeiss, Oberkochen, Germany) operated at 15 kV. The conducting Au atoms were sputtered on the specimen surface for SEM observations. XRD Rietveld refinements were conducted with the General Structure Analysis System (GSAS) program. The 532 nm and 785 nm lasers were used for excitation to obtain the Raman spectra (RS) of the ceramics and photoluminescence (PL) of Ho^{3+} using a LabRAM XploRA Raman spectrometer (Horiba Jobin Yvon, Longjumeau, France). X-ray photoelectron spectroscopy (XPS, ESCA-LAB250) measurements were performed to study the valence states of cations. The measurement curves of XPS data were fitted by a mixed Gaussian–Lorentzian function, and Shirley-type background subtraction was used. EPR measurements were carried out with an X-band (≈9.4 GHz) spectrometer (A300, Bruker, Rheinstetten, Germany) at 90–298 K. The gyromagnetic constant (g) was calculated using $hv = g\mu_0 H$, where h is the Planck constant ($h = 6.626 \times 10^{-34}$ J·s), v is the microwave frequency, μ_0 is the Bohr magnetron ($\mu_0 = 9.262 \times 10^{-24}$ J/T), and H is the magnetic field strength. The dielectric properties of the ceramic samples were measured on a broadband dielectric spectrometer (Concept 41, Novocontrol Technologies, Montabaur Germany) in a temperature range of 198–473 K and a frequency range of 1 Hz–10 MHz.

4. Conclusions

Converting renewable energy to electricity and efficient electricity storage are keys to addressing the energy crisis. $BaTiO_3$ dielectric capacitors are critical energy storage devices due to their ultrafast charge/discharge ability, exceptional cycle life and high-temperature tolerance. However, the unstable and low dielectric constant (ε'_{RT} = 1600) near the room temperature of $BaTiO_3$ ceramics cannot meet the needs of miniaturization and the high capacity of dielectric capacitors. In this work, Gd^{3+} and Ho^{3+} codoped tetragonal $BaTiO_3$ ceramics were prepared by carefully adjusting the synthesis conditions to address this issue. The optimal ceramic sintered at 1400 °C for 6 h had an ultrahigh room-temperature dielectric constant (ε'_{RT} = 5475) with low dielectric loss (tan δ = 0.0176). In addition, the BGTH7 ceramic exhibits good X7U dielectric properties in the temperature range of −55~125 °C, which is superior to other X7U $BaTiO_3$-based ceramics reported previously. The mechanisms for improving dielectric properties can be attributed to the tetragonal perovskite structure, large grain size, and the formation of the $\mathrm{Gd}_{\mathrm{Ba}}^{\bullet}$-$\mathrm{Ho}_{\mathrm{Ti}}^{\prime}$ complex. The high capacitance of this ceramic helps reduce the capacitor size, improve the efficiency, and enable miniature applications. The BGTH7 ceramic can be prepared as dielectric capacitors with high capacitance, is widely used in pulse power devices, hybrid automotive power supplies, and other fields, and will be beneficial to many portable electronic applications. In addition, the ceramic exhibits wide temperature range stability and is suitable for applications in extreme environments such as polar, high altitude, and underground tunnels.

Supplementary Materials: The following supporting information can be downloaded at: https://www.mdpi.com/article/10.3390/molecules27217464/s1, Figure S1: SEM images of the surface for BGTH7 ceramics with different T_s (a) T_s = 1200 °C, (b) T_s = 1300 °C, (c) T_s = 1400 °C for 12 h.; Figure S2: The grain size analysis of the BGTH7 ceramics of BGTH7 ceramics sintered for (a) 1 h (b) 3 h and (c) 12 h at 1400 °C; Figure S3: Ti 2p XPS spectra of BGTH7 ceramics sintered for (a) 1 h (b) 3 h (c) 12 h at 1400 °C; Figure S4: EPR spectra of BGTH7 ceramics sintered at different T_s for 12 h measured at room temperature; Figure S5: Raman spectra under 532 nm excitation of ceramics sintered at different T_s for 12 h measured at room temperature; Figure S6: Temperature dependence of the dielectric constant (ε') and the dielectric loss (tan δ) for ceramics sintered at T_s = 1200 °C, 1300 °C and 1400 °C; Figure S7: Frequency dependence of the dielectric permittivity (ε') and the dielectric loss (tan δ) for BGTH7 ceramics sintered at T_s = 1200 °C, 1300 °C and 1400 °C; Figure S8: ε'_{RT} and tan δ at room temperature vary with grain size (GS) and relative density (ρ_r) for BGTH7 ceramics sintered at 1400 °C; Figure S9: Dielectric peak temperature varies with dwell time for BGTH7 ceramics sintered at 1400 °C; Table S1: Rietveld Refined lattice parameters of BGTH7 ceramics sintered at 1400 °C; Table S2: Ionic radii as a function of coordinate number (CN); Table S3: EIA Definition of Class II Capacitors; Table S4: Dielectric properties of all BGTH7 ceramics; Table S5: The dielectric properties of this work are compared with those of previously reported $BaTiO_3$-based dielectric ceramics with X7U specifications.

Author Contributions: Conceptualization, J.B.; methodology, L.L., J.B. and Q.L.; investigation, J.B.; resources, L.L. and Q.L.; writing—original draft preparation, J.B.; writing—review and editing, J.B., L.L., X.L., Q.L. and X.W.; supervision, L.L. and X.L. All authors have read and agreed to the published version of the manuscript.

Funding: This work was supported by the National Natural Science Foundation of China (Grant Nos. 22175070 and 21771075), and the Jilin Provincial Department of Science and Technology (Grant No. 20200801034GH).

Institutional Review Board Statement: Not applicable.

Informed Consent Statement: Not applicable.

Data Availability Statement: Not applicable.

Acknowledgments: The first author expresses their deep gratefulness to Dayong Lu for his supervision of the design of the initial experimental process.

Conflicts of Interest: The authors declare no conflict of interest.

References

1. Zhou, M.; Liang, R.; Zhou, Z.; Dong, X. Novel $BaTiO_3$-based lead-free ceramic capacitors featuring high energy storage density, high power density, and excellent stability. *J. Mater. Chem. C* **2018**, *6*, 8528–8537. [CrossRef]
2. Wang, X.; Ren, P.; Wang, J.; Xu, J.; Xi, Y. Multi-phase coexistence and temperature-stable dielectric properties in $BaTiO_3$/ZnO composite ceramics. *J. Eur. Ceram. Soc.* **2020**, *40*, 1896–1901. [CrossRef]
3. Tawade, B.; Apata, I.; Pradhan, N.; Karim, A.; Raghavan, D. Recent Advances in the Synthesis of Polymer-Grafted Low-K and High-K Nanoparticles for Dielectric and Electronic Applications. *Molecules* **2021**, *26*, 2942. [CrossRef] [PubMed]
4. Boonlakhorn, J.; Manyam, J.; Srepusharawoot, P.; Krongsuk, S.; Thongbai, P. Effects of charge compensation on colossal permittivity and electrical properties of grain boundary of $CaCu_3Ti_4O_{12}$ ceramics Substituted by Al^{3+} and Ta^{5+}/Nb^{5+}. *Molecules* **2021**, *26*, 3294. [CrossRef] [PubMed]
5. Liu, C.; Li, F.; Ma, L.P. Advanced materials for energy storage. *Adv. Mater.* **2010**, *22*, E28–E62. [CrossRef]
6. Zhou, H.Y.; Zhu, X.N.; Ren, G.R.; Chen, X.M. Enhanced energy storage density and its variation tendency in $CaZr_xTi_{1-x}O_3$ ceramics. *J. Alloy Compd.* **2016**, *688*, 687–691. [CrossRef]
7. Bokov, A.; Ye, Z.-G. Recent progress in relaxor ferroelectrics with perovskite structure. *J. Mater. Sci.* **2006**, *41*, 31–52. [CrossRef]
8. Hong, K.; Lee, T.H.; Suh, J.M.; Yoon, S.-H.; Jang, H.W. Perspectives and challenges in multilayer ceramic capacitors for next generation electronics. *J. Mater. Chem. C* **2019**, *7*, 9782–9802. [CrossRef]
9. Jiang, B.; Iocozzia, J.; Zhao, L.; Zhang, H.; Harn, Y.-W.; Chen, Y.; Lin, Z. Barium titanate at the nanoscale: Controlled synthesis and dielectric and ferroelectric properties. *Chem. Soc. Rev.* **2019**, *48*, 1194–1228. [CrossRef]
10. Saini, P.; Arora, M.; Gupta, G.; Gupta, B.K.; Singh, V.N.; Choudhary, V. High permittivity polyaniline-barium titanate nanocomposites with excellent electromagnetic interference shielding response. *Nanoscale* **2013**, *5*, 4330–4336. [CrossRef]
11. Jia, H.; Chen, J. Tailoring the tetragonal distortion to obtain high Curie temperature and large piezoelectric properties in $BiFeO_3$-$PbTiO_3$-$BaTiO_3$ solid solutions. *J. Eur. Ceram. Soc.* **2020**, *41*, 2443–2449. [CrossRef]
12. Xie, Y.; Yin, S.; Hashimoto, T.; Tokano, Y.; Sasaki, A.; Sato, T. Low temperature synthesis of tetragonal $BaTiO_3$ by a novel composite-hydroxide-mediated approach and its dielectric properties. *J. Eur. Ceram. Soc.* **2010**, *30*, 699–704. [CrossRef]
13. Ma, R.; Cui, B.; Shangguan, M.; Wang, S.; Wang, Y.; Chang, Z.; Wang, Y. A novel double-coating approach to prepare fine-grained BaTiO3@La2O3@SiO2 dielectric ceramics for energy storage application. *J. Alloy. Compd.* **2017**, *690*, 438–445. [CrossRef]
14. Jin, S.H.; Lee, H.W.; Kim, N.W.; Lee, B.-W.; Lee, G.-G.; Hong, Y.-W.; Nam, W.H.; Lim, Y.S. Sonochemically activated solid-state synthesis of BaTiO3 powders. *J. Eur. Ceram. Soc.* **2021**, *41*, 4826–4834. [CrossRef]
15. Ben, L.; Sinclair, D.C. Anomalous Curie temperature behavior of A-site Gd-doped BaTiO3 ceramics: The influence of strain. *Appl. Phys. Lett.* **2011**, *98*, 092907. [CrossRef]
16. Han, F.; Bai, Y.; Qiao, L.-J.; Guo, D. A systematic modification of the large electrocaloric effect within a broad temperature range in rare-earth doped $BaTiO_3$ ceramics. *J. Mater. Chem. C* **2016**, *4*, 1842–1849. [CrossRef]
17. Huang, Q.; Si, F.; Tang, B. The effect of rare-earth oxides on the energy storage performances in $BaTiO_3$ based ceramics. *Ceram. Int.* **2022**, *48*, 17359–17368. [CrossRef]
18. Jeon, S.-C.; Kang, S.-J.L. Coherency strain enhanced dielectric-temperature property of rare-earth doped $BaTiO_3$. *Appl. Phys. Lett.* **2013**, *102*, 112915. [CrossRef]
19. Hu, W.; Chen, Z.; Lu, Z.; Wang, X.; Fu, X. Effect of Bi2O3 and Ho2O3 co-doping on the dielectric properties and temperature reliability of X8R BaTiO3-based ceramics. *Ceram. Int.* **2021**, *47*, 24982–24987. [CrossRef]
20. Lu, D.Y.; Guan, D.X.; Li, H.B. Multiplicity of photoluminescence in Raman spectroscopy and defect chemistry of $(Ba_{1-x}R_x)(Ti_{1-x}Ho_x)O_3$ (R = La, Pr, Nd, Sm) dielectric ceramics. *Ceram. Int.* **2018**, *44*, 1483–1492. [CrossRef]
21. Lu, D.-Y.; Gao, X.-L.; Wang, S. Abnormal Curie-temperature shift in Ho-doped BaTiO3 ceramics with the self-compensation mode. *Results Phys.* **2018**, *12*, 585–591. [CrossRef]
22. Yuan, L.; Hu, W.; Fang, S.; Li, G.; Wang, X.; Wu, X.; Li, L. CdO-CuO-TiO_2 ternary dielectric systems: Subsolidus phase diagram and the effects of Cu segregation. *J. Eur. Ceram. Soc.* **2018**, *38*, 4978–4985. [CrossRef]
23. Tsuji, K.; Ndayishimiye, A.; Lowum, S.; Floyd, R.; Wang, K.; Wetherington, M.; Maria, J.-P.; Randall, C.A. Single step densification of high permittivity $BaTiO_3$ ceramics at 300 °C. *J. Eur. Ceram. Soc.* **2019**, *40*, 1280–1284. [CrossRef]
24. Wang, H.; Li, G.; Li, L. Molten-salt-mediated synthesis and low-temperature electrical conduction of $LnCoO_3$ (Ln=Pr, Nd, Sm, and Gd). *J. Alloy Compd.* **2014**, *612*, 227–232. [CrossRef]
25. Wang, X.; Deng, X.; Wen, H.; Li, L. Phase transition and high dielectric constant of bulk dense nanograin barium titanate ceramics. *Appl. Phys. Lett.* **2006**, *89*, 162902. [CrossRef]
26. Manika, G.C.; Andrikopoulos, K.S.; Psarras, G.C. On the ferroelectric to paraelectric structural transition of $BaTiO_3$ micro-/nanoparticles and their epoxy nanocomposites. *Molecules* **2020**, *25*, 2686. [CrossRef] [PubMed]
27. Naik, R.; Nazarko, J.J.; Flattery, C.S.; Venkateswaran, U.D.; Naik, V.M. Temperature dependence of the Raman spectra of polycrystalline $Ba_{1-x}Si_xTiO_3$. *Phys. Rev. B* **2000**, *61*, 11367–11372. [CrossRef]
28. Lin, M.-F.; Thakur, V.K.; Tan, E.J.; Lee, P.S. Dopant induced hollow $BaTiO_3$ nanostructures for application in high performance capacitors. *J. Mater. Chem.* **2011**, *21*, 16500–16504. [CrossRef]
29. Petrovsky, V.; Petrovsky, T.; Kamlapurkar, S.; Dogan, F. Dielectric Constant of Barium Titanate Powders Near Curie Temperature. *J. Am. Ceram. Soc.* **2008**, *91*, 3590–3592. [CrossRef]

30. Ma, N.; Zhang, B.P.; Yang, W.G.; Guo, D. Phase structure and nano-domain in high performance of $BaTiO_3$ piezoelectric ceramics. *J. Eur. Ceram. Soc.* **2012**, *32*, 1059–1066. [CrossRef]
31. Alkathy, M.S.; Hezam, A.; Manoja, K.; Wang, J.; Cheng, C.; Byrappa, K.; Raju, K.J. Effect of sintering temperature on structural, electrical, and ferroelectric properties of lanthanum and sodium co-substituted barium titanate ceramics. *J. Alloy Compd.* **2018**, *762*, 49–61. [CrossRef]
32. Song, Y.; Wang, X.; Zhang, X.; Sui, Y.; Zhang, Y.; Liu, Z.; Lv, Z.; Wang, Y.; Xu, P.; Song, B. The contribution of doped-Al to the colossal permittivity properties of $Al_xNb_{0.03}Ti_{0.97}$-xO_2 rutile ceramics. *J. Mater. Chem. C* **2016**, *4*, 6798–6805. [CrossRef]
33. Gao, B.; Xu, S.; Xu, Q. CO_2 Induced Exposure of the Intrinsic Magnetic Surface of $BaTiO_3$ to Give Room-Temperature Ferromagnetism. *Angew. Chem. Int. Ed. Engl.* **2022**, *61*, e202117084. [CrossRef]
34. Lu, D.Y.; Liu, T.T. Dielectric properties and defect chemistry of $(Ba_{1-x}La_x)(Ti_{1-x}Lu_x)O_3$ ceramics. *J. Alloys Compd.* **2017**, *698*, 967–976. [CrossRef]
35. Kolodiazhnyi, T.; Petric, A. Analysis of point defects in polycrystalline BaTiO3 by electron paramagnetic resonance. *J. Phys. Chem. Solids* **2003**, *64*, 953–960. [CrossRef]
36. Munteanu, A.-C.; Badea, M.; Olar, R.; Silvestro, L.; Dulea, C.; Negut, C.-D.; Uivarosi, V. Synthesis and Structural Investigation of New Bio-Relevant Complexes of Lanthanides with 5-Hydroxyflavone: DNA Binding and Protein Interaction Studies. *Molecules* **2016**, *21*, 1737. [CrossRef]
37. Singh, V.; Singh, N.; Watanabe, S.; Rao, T.K.G.; Pathak, M.S.; Srivastava, A.K.; Singh, P.K.; Dhoble, S.J. Gadolinium-Activated CaZr4O9 Ultraviolet-B-Emitting Phosphor: A Luminescence and EPR Study. *J. Electron. Mater.* **2017**, *46*, 1943–1947. [CrossRef]
38. Aminov, L.K.; Kurkin, I.N.; Malkin, B.Z. Superhyperfine structure in the EPR spectra and optical spectra of impurity f ions in dielectric crystals: A review. *Phys. Solid State* **2013**, *55*, 1343–1363. [CrossRef]
39. Lu, D.-Y.; Guan, D.-X. Photoluminescence associated with the site occupations of Ho_3+ ions in $BaTiO_3$. *Sci. Rep.* **2017**, *7*, 6125. [CrossRef]
40. Pan, M.J.; Randall, C.A. A brief introduction to ceramic capacitors. *Electr. Insul. M.* **2010**, *26*, 44. [CrossRef]
41. Tavernor, A.W.; Lia, H.-P.S.; Stevens, R. Production and characterisation of composite relaxor ferroelectric multi-layer structures. *J. Eur. Ceram. Soc.* **1999**, *19*, 1859. [CrossRef]
42. Furukawa, O.; Harata, M.; Imai, M.; Yamashita, Y.; Mukaeda, S. Low firing and high dielectric constant X7R ceramic dielectric for multilayer capacitors based on relaxor and barium titanate composite. *J. Mater. Sci.* **1991**, *26*, 5838. [CrossRef]
43. Hino, T.; Matsumoto, N.; Nishida, M.; Araki, T. PLD of X7R for thin film capacitors. *Appl. Surf. Sci.* **2008**, *254*, 2638. [CrossRef]
44. Lu, D.Y.; Peng, Y.Y.; Yu, X.Y.; Sun, X.Y. Dielectric properties and defect chemistry of La and Tb co-doped $BaTiO_3$ ceramics. *J. Alloys Compd.* **2016**, *681*, 128–138. [CrossRef]
45. Zhao, Y.; Wang, Q.; Lv, J.-H.; Zhao, X.; Wang, C.-M. Dielectric properties and electrocaloric effect of yttrium-modified BaTiO3 ceramics. *Ceram. Int.* **2021**, *47*, 18610–18618. [CrossRef]
46. Lu, D.Y.; Liang, Y. Valence states and dielectric properties of fine-grained $BaTiO_3$ ceramics co-doped with double valence-variable europium and chromium. *Ceram. Int.* **2018**, *44*, 14717–14727. [CrossRef]
47. Liu, M.; Hao, H.; Zhen, Y.; Wang, T.; Zhou, D.; Liu, H.; Cao, M.; Yao, Z. Temperature stability of dielectric properties for xBiAlO$_3$-$(1-x)$BaTiO$_3$ ceramics. *J. Eur. Ceram. Soc.* **2015**, *35*, 2303–2311. [CrossRef]
48. Turcan, I.; Lukacs, V.A.; Curecheriu, L.; Padurariu, L.; Ciomaga, C.E.; Airimioaei, M.; Stoian, G.; Lupu, N.; Mitoseriu, L. Microstructure and dielectric properties of Ag-$BaTiO_3$ composite ceramics. *J. Eur. Ceram. Soc.* **2018**, *38*, 5420–5429. [CrossRef]
49. Li, J.; Pu, Y.; Shi, Y.; Shi, R.; Wang, X.; Yang, M.; Wang, W.; Guo, X.; Peng, X. Dielectric, multiferroic and magnetodielectric properties of $(1\text{-}x)BaTiO_3$-xSr_2CoMoO_6 solid solution. *Ceram. Int.* **2019**, *45*, 16353–16360. [CrossRef]
50. Haily, E.; Bih, L.; El Bouari, A.; Lahmar, A.; Elmarssi, M.; Manoun, B. Effect of BaO-Bi_2O_3-P_2O_5 glass additive on structural, dielectric and energy storage properties of $BaTiO_3$ ceramics. *Mater. Chem. Phys.* **2020**, *241*, 123034. [CrossRef]
51. Fan, T.; Ji, C.; Chen, G.; Cai, W.; Gao, R.; Deng, X.; Wang, Z.; Fu, C. Enhanced the dielectric relaxation characteristics of $BaTiO_3$ ceramic doped by $BiFeO_3$ and synthesized by the microwave sintering method. *Mater. Chem. Phys.* **2020**, *250*, 123034. [CrossRef]
52. Wan, Y.; Tang, L.; Dang, X.; Ren, P.; Ma, M.; Song, K.; Zhao, G. High temperature dielectrics based on $Bi_{1/2}Na_{1/2}TiO_3$-$BaTiO_3$-$Sr_{0.53}Ba_{0.47}Nb_2O_6$ ceramics with high dielectric permittivity and wide operational temperature range. *Ceram. Int.* **2019**, *45*, 2596–2601. [CrossRef]
53. Chen, X.; Huang, G.; Ma, D.; Liu, G.; Zhou, H. High thermal stability and low dielectric loss of $BaTiO_3$-$Bi(Li_{1/3}Zr_{2/3})O_3$ solid solution. *Ceram. Int.* **2017**, *43*, 926–929. [CrossRef]
54. Ma, J.P.; Chen, X.M.; Ouyang, W.Q.; Wang, J.; Li, H.; Fang, J.-L. Microstructure, dielectric, and energy storage properties of $BaTiO_3$ ceramics prepared via cold sintering. *Ceram. Int.* **2018**, *44*, 4436–4441. [CrossRef]
55. Chen, W.; Hao, H.; Yang, Y.; Chen, C.; Appiah, M.; Yao, Z.; Cao, M.; Yu, Z.; Liu, H. Dielectric properties and impedance analysis of $BaTiO_3$ -based ceramics with core-shell structure. *Ceram. Int.* **2017**, *43*, 8449–8458. [CrossRef]
56. Meng, K.; Li, W.; Tang, X.G.; Liu, Q.X.; Jiang, Y.P. A review of a good binary ferroelectric ceramic: $BaTiO_3$–$BiFeO_3$. *ACS Appl. Electron. Mater.* **2021**, *4*, 2109–2145. [CrossRef]
57. Ghayour, H.; Abdellahi, M. A brief review of the effect of grain size variation on the electrical properties of $BaTiO_3$-based ceramics. *Powder Technol.* **2016**, *292*, 84–93. [CrossRef]
58. Buscaglia, V.; Randall, C.A. Size and scaling effects in barium titanate. An overview. *J. Eur. Ceram. Soc.* **2020**, *40*, 3744–3758. [CrossRef]

59. Freeman, C.L.; Dawson, J.A.; Harding, J.H.; Ben, L.B.; Sinclair, D.C. The Influence of A-Site Rare Earth Ion Size in Controlling the Curie Temperature of $Ba_{1-x}RE_xTi_{1-x/4}O_3$. *Adv. Funct. Mater.* **2013**, *23*, 491–495. [CrossRef]
60. Khedhri, M.H.; Abdelmoula, N.; Khemakhem, H.; Douali, R.; Dubois, F. Structural, spectroscopic and dielectric properties of Ca-doped $BaTiO_3$. *Appl. Phys. A* **2019**, *125*, 1–13. [CrossRef]
61. Martirenat, H.T.; Burfoot, J.C. Grain-size effects on properties of some ferroelectric ceramics. *J. Phys. C Solid State Phys.* **1974**, *7*, 3182–3192. [CrossRef]
62. Zhang, Q.W.; Zhai, J.W.; Shen, B.; Zhang, H.J.; Yao, X. Grain size effects on dielectric properties of barium strontium titanate composite ceramics. *Mater. Res. Bull.* **2013**, *48*, 973–977. [CrossRef]